

Electron Emission Area Depends on Electric Field and Unveils Field Emission Properties in Nanodiamond Films

Oksana Chubenko^{1,2,*}, Stanislav S. Baturin³, Kiran Kumar Kovi², Anirudha V. Sumant⁴, and Sergey V. Baryshev^{2†}

¹*Department of Physics, The George Washington University,
725 21st St. NW, Washington, DC 20052, USA*

²*Euclid TechLabs, 365 Remington Blvd., Bolingbrook, IL 60440, USA*

³*PSD Enrico Fermi Institute, The University of Chicago, 5640 S. Ellis Ave, Chicago, IL 60637, USA*

⁴*Center for Nanoscale Materials, 9700 S. Cass Ave., Argonne, IL 60439, USA*

In this paper we study the effect of actual, locally resolved, field emission (FE) area on electron emission characteristics of uniform semimetallic nitrogen-incorporated ultrananocrystalline diamond ((N)UNCD) field emitters. To obtain the actual FE area, imaging experiments were carried out in a vacuum system in a parallel-plate configuration with a specialty anode phosphor screen. Electron emission micrographs were taken concurrently with I - V characteristics measurements. It was found that in uniform (N)UNCD films the field emitting site distribution is not uniform across the surface, and that the actual FE area depends on the applied electric field.

To quantify the actual FE area dependence on the applied electric field, a novel automated image processing algorithm was developed. The algorithm processes extensive imaging datasets and calculates emission area per image. By doing so, it was determined that the emitting area was always significantly smaller than the FE cathode surface area of 0.152 cm^2 available. Namely, the actual FE area would change from $5 \times 10^{-3} \%$ to 1.5% of the total cathode area with the applied electric field increased.

We also found that (N)UNCD samples deposited on stainless steel with molybdenum and nickel buffer layers always had better emission properties with the turn-on electric field $< 5 \text{ V}/\mu\text{m}$ and β -factor of about 1,000, as compared to those deposited directly onto tungsten having the turn-on field $> 10 \text{ V}/\mu\text{m}$ and β -factor of about 200. It was concluded that rough or structured surface, either on the macro- or micro- scale, is not a prerequisite for good FE properties. Raman spectroscopy suggested that increased amount of the graphitic sp^2 phase, manifested as reduced D/G peak ratio, was responsible for improved emission characteristics.

Finally and most importantly, it was shown that when I - E curves as measured in the experiment were normalized by the field-dependent emission area, the resulting j - E curves demonstrated a strong kink and significant deviation from Fowler-Nordheim (FN) law, and eventually saturated at a current density of $\sim 100 \text{ mA}/\text{cm}^2$. This value was nearly identical for all studied (N)UNCD films, regardless of the substrate.

I. INTRODUCTION

In general, the electron field emission (FE) properties and thus efficiency of field emitters are evaluated by plotting the current density as a function of the applied electric field E (linear j - E plot representation). For the parallel-plate electrodes configuration, E is simply a product of the applied voltage V over inter-electrode gap d . j is a product of I over S , where I is the current measured in experiment and S is the emitting surface area. The experimentally determined current density j is compared to the current density predicted by the Fowler-Nordheim (FN) law that can be written in a simplified form proposed by Millikan $j(E) \sim E^2 \exp(-k/E)$, with $k \propto \frac{\phi^{3/2}}{\beta}$, and ϕ being the work function and β being the field enhancement factor, so called β -factor. The FN law was originally developed to describe FE from an ideal flat metallic surface in an ultrahigh electric field $\sim 1 \text{ GV}/\text{m}$ at 0 K [1]. In many instances, it is convenient to present properties of field emitters in $\ln(j/E^2)$ vs. $1/E$ coordinates (so-called FN plot representation). This helps understand whether a field emitter under study obeys the

FN law, as well as to calculate the β -factor from the linear slope k . As seen, both j - E plot and FN plot involve the current density rather than the apparent, as measured, current, which makes the emission area an important parameter to characterize FE properties of materials.

Conventionally, the normalization of the apparent current I by the emission area S is done by using the entire surface area of a field emission cathode exposed to the electric field (cathode smaller than anode) or by the entire size of an anode collecting current in the middle of a cathode (anode is smaller than cathode) [2]. This has been the standard approach for parallel-plate configuration FE measurement systems. In either of the ways of, a small cathode with the area S facing a large anode or a small anode with the area S collecting electrons from a part of a large cathode, S is always assumed to be constant. Having S constant is in contrast to locally-resolved FE characteristics of arrays and patterned/structured surfaces of semiconductors (e.g. Si and GaN) vastly reported by the groups working collaboratively at the University of Wuppertal and the Regensburg University of Applied Sciences [3, 4]. In those experiments, a micron-

size anode was scanned across areas of interest with the gap kept constant. At each location, the applied voltage was increased or decreased (depending on the location emissivity) in order to set the emitted current to 1 nA, and 3D maps (x -coordinate, y -coordinate, V) were recorded. The main result was that V can vary by a factor of 2 to 3 across the area of interest. These findings suggested that the emission area S had to change with V in experiments when the micron-size anode would be replaced with a large plate electrode. This situation can also be referred to as a problem of non-uniform (strong and weak) emitters.

Eventually, the convention of using the constant emission area: (i) makes it difficult not only to compare emission characteristics between different field emitters, but even between those of the same sample when such a sample undergoes various treatments or modifications and (ii) may lead to inadequate interpretation of experimental results. Attempts to avoid the use of S and representation of field emission data by plotting the as-measured current I against applied voltage is also a cumbersome approach as it has no unification between diverse experimental setups.

Similar to the mentioned locally resolved emission properties of Si and GaN emitters [3, 4], there were a few reports on non-uniform emission from carbonic materials such as carbon nanotubes (CNT) [5, 6] and synthetic nanodiamond films [7]. Emphasis is given to these materials as CNT and synthetic polycrystalline diamond have long been acknowledged as promising FE electron sources [8]. They are efficient and simple to synthesize and scale. While exceptionally high efficiency of CNT is largely a consequence of their exceptionally high aspect ratios, nitrogen-incorporated ultrananocrystalline diamond ((N)UNCD), a highly conductive type of nanodiamond[9], is an unconventional field emitter that performs simply in planar thin film configuration and has turn-on fields ~ 10 V/ μm , far below breakdown threshold for any material. Nonetheless, in Refs. [5–7] no attempts to quantify the actual FE area and to establish the dependence of the FE area on the applied electric field (if any) have been made. In this paper, we describe a novel approach to measure FE site distribution, laterally-resolved on the cathode surface, and to quantify it by obtaining the dependence of S on the electric field. This approach was applied to planar thin film (N)UNCD field emitters grown on stainless steel and tungsten.

II. EXPERIMENT

The experiments were performed in a custom imager in the parallel-plate configuration as described in Ref.[10]. For convenience, the measurement setup is shown in Fig.1. The imager has a specialty anode screen which is an optically polished (1 inch dia. and 100 μm thick) disk

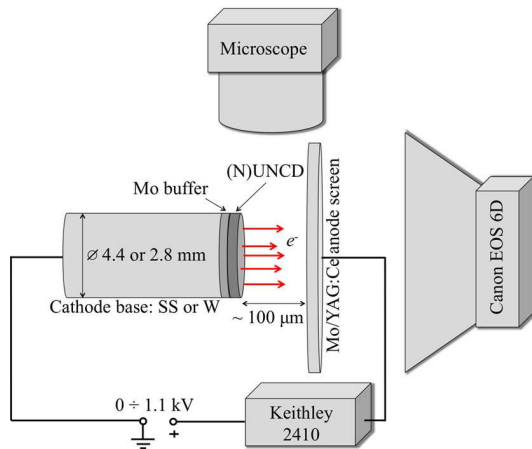


FIG. 1: Measurement setup diagram (not to scale).

made of yttrium aluminum garnet doped with cerium (YAG:Ce) coated with a Mo film of about 7-8 nm in thickness. The distance between the sample and the anode screen is set using a micrometer holding the sample. Top and side view cameras outside the vacuum (side view camera is not depicted in Fig.1) are used to check the parallelism between the cathode and anode, and to measure the gap. A Canon DLSR camera is installed at a viewport behind the anode screen to take pictures of electron emission patterns, which are formed via cathodoluminescence (YAG:Ce has 550 nm luminescence line) when electrons, emitted from the sample and accelerated to the energy equal to the voltage applied between the electrodes, strike the YAG:Ce anode screen. Patterns of cathodoluminescence formed on the YAG:Ce anode screen placed ~ 100 μm away from the cathode represent field electron emission from the sample. The sample electrode is at ground and the anode frame is isolated and positively biased. The bias and current readings are enabled by a Keithley 2410 electrometer. Dwell time at each point to acquire simultaneously the current and voltage values with their errors, the vacuum pressure reading and a micrograph is about 5 seconds. The voltage is swept up and down with a step 1 V from 0 to 1.1 kV. Therefore, the total time per fully automated experiment is approximately 3 hours.

To look at the entire cathode surface area, the cathodes were purposely made smaller than the imaging Mo/YAG:Ce anode screen which is 1 inch in diameter. The anodes used were 316 stainless steel (SS) cylinder samples 4.4 mm in diameter, and tungsten cylinder sample 2.8 mm in diameter. The SS substrate cylinders were optically polished and the W cylinder substrate had macroscopic roughness (Fig.2a).

(N)UNCD films were grown using a standard procedure which was established in our previous studies using a microwave-assisted chemical vapor deposition system in a mixture of $\text{CH}_4/\text{Ar}/\text{N}_2$ with small addition of H_2 for initial plasma ignition [11, 12]. To grow (N)UNCD

on the SS substrates, Mo buffer of approximately 110 nm was deposited on SS by magnetron sputtering. Base pressure in the magnetron system was $< 5 \times 10^{-7}$ Torr. Prior to coating, the SS cylinders were cleaned *in situ* using RF discharge plasma. Without breaking vacuum, immediately after the cleaning, the Mo coating was deposited. Ar was used as a working gas for both cleaning and sputtering at a pressure of $\sim 10^{-3}$ Torr. In addition, to vary surface morphology one Mo/SS was finished with ~ 10 nm Ni film that was deposited in the same magnetron system. We observed that under the same growth conditions, Ni induced the (N)UNCD film to consist of densely packed spheres (Fig.2b).

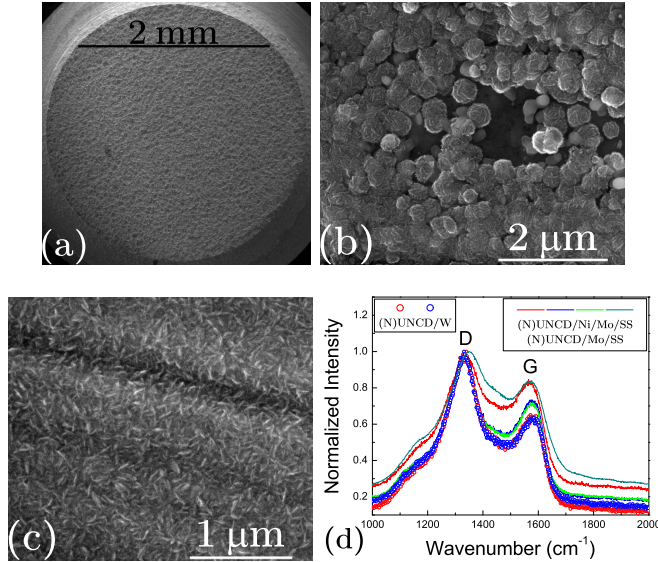


FIG. 2: SEM micrographs of (a) the original macroscopic surface roughness of the W substrate; (b) the final morphology of the (N)UNCD/Ni/Mo/SS sample; (c) needle-like (N)UNCD topography, identical to all (N)UNCD films regardless of the substrate or buffer layers; (d) Raman spectra of the samples, showing high variation (between the samples and across the surface of the same sample) in the D/G ratio.

All (N)UNCD films had nearly identical topography as seen by scanning electron microscopy (SEM), i.e. they had needlelike nanostructure as illustrated in Fig.2c. Raman spectroscopy performed using a He-Ne laser ($\lambda=633$ nm) on the other hand revealed difference between the films on different substrates. From Fig.2d, it follows that the D/G ratio was 1.2 to 1.4 for the (N)UNCD on the SS substrates while the D/G was 1.6 for the (N)UNCD on tungsten. Smaller D/G ratio suggests higher content of graphitic sp^2 phase in (N)UNCD. This behavior is consistent to the previous studies as reported in Refs.[13–15]. This is also consistent with our previous measurements: an (N)UNCD film on pure Mo substrate featured a D/G=1.6 [11], while an (N)UNCD on Mo/SS had a D/G=1.3 [12]. The resistivity of the (N)UNCD films is assumed to be $0.1 \Omega \times \text{cm}$, as suggested by a four-probe

measurement of a (N)UNCD film grown on an insulating Si witness coupon under the same growth conditions.

III. RESULTS AND DISCUSSIONS

Four datasets obtained from the measurements are presented here: one from (N)UNCD/Mo/SS emitter, two sets taken at different inter-electrode gaps (147 and 106 μm) from (N)UNCD/Ni/Mo/SS emitter, and one set from (N)UNCD/W emitter (we will further label the datasets as **MoSS**, **NiMoSS1**, **NiMoSS2**, and **W**, respectively). Fig.3, showing one image per dataset, illustrates emission patterns captured by the camera behind the Mo/YAG:Ce anode screen (see Fig.1) – the green light patterns are caused by the process of cathodoluminescence when field emitted electrons accelerated to a few hundred or a thousand eV bombard the phosphor. This means the patterns represent field electron emission from (N)UNCD cathode projected onto the Mo/YAG:Ce anode screen placed $\sim 100 \mu\text{m}$ away from the cathode. Comparing results presented in Fig.3, our initial qualitative conclusions were that (i) the field emission site distribution in topographically uniform (N)UNCD thin films is not uniform and (ii) the (N)UNCD samples grown on the SS base would emit larger currents with emission distributed more uniformly as compared to the (N)UNCD on the W base.

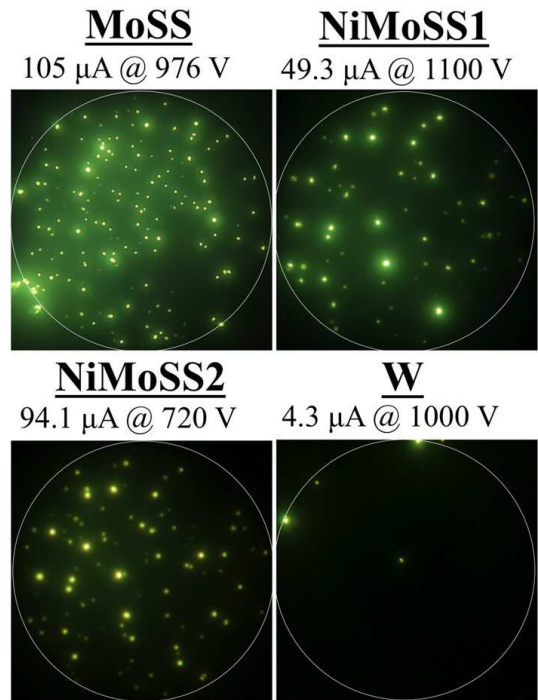


FIG. 3: Imaging chart of the four imaging datasets obtained from the FE measurements. The chart compares emissivity of the samples at the maximal electric field and current.

To enable accurate quantitative analysis of the extensive FE micrograph datasets described and discussed below, we made use of a clustering-based algorithm class. Such algorithms, for instance, are common tools in quantitative image analyses in astrophysics [16] and biology [17] used for accurate discrimination of a true signal from the background. The procedure in its entirety is explained in Appendix A and the core concept is mentioned in brief here. The core concept of the method is based on digitization of FE imaging micrographs and partitioning of resulting data into groups, or clusters, of similar elements. The image-clustering algorithms are adapted as required by using the strategies and approaches as described in [18–20]. The entire analysis procedure is implemented in Wolfram Mathematica to run in a parallel configuration on a multi-core computing cluster such that each processor is dedicated to work on its prescribed image. By doing so, it becomes possible to process about 100 images concurrently; reducing the total computation time dramatically. This method does not require a priori knowledge about the number and shape of clusters and can be used as an automated cathode performance test. The pixel size in cm^2 is referenced to the full image size in pixels and the known diameter of the (N)UNCD cathode, 0.44 or 0.28 cm. The product of the total number of pixels combined by the clustering procedure and the pixel size in cm^2 provides the total emission area per micrograph in the datasets shown in the Appendices B to E. As a specific example of how an image is converted into a pixel map of a known field emission area, we use a micrograph from the dataset **MoSS**, 21.8 μA @650V, Appendix B. The width of the image in pixels is equal to the sample diameter d , with $d = 0.44$ cm, which allows for calculating a single pixel area S_{pix} as small as $9.9 \times 10^{-7} \text{ cm}^2$. Multiplication of the total number of selected pixels by S_{pix} yields the total emission area of $4 \times 10^{-4} \text{ cm}^2$ (Fig.4).

The set **MoSS** was measured manually starting at 3.8 V/ μm when reasonably bright YAG:Ce emission was detected with the camera at ISO=1,000 and a shutter speed of 1 second. After that, images were taken every 50 V until the maximum current of 100 μA was reached. Therefore, there are 11 "current-voltage-image" measurements in this case (see Appendix B).

For other samples/sets, our most recent LabVIEW software was configured such that the imaging camera took images every 20 V (sets **NiMoSS1** and **NiMoSS2** in Appendices C and D) and 10 V (set **W**, Appendix E) as voltage was first ramped up and then down. I - V measurements for all sets **NiMoSS1**, **NiMoSS2** and **W** were performed with a step of 1 V. All image datasets (see appendices) were processed using the automated algorithm, as described is Appendix A, further to evaluate the actual FE area and determine its dependence on the electric field, $S_{loc}(E)$.

For all four datasets in discussion, we plotted the cur-

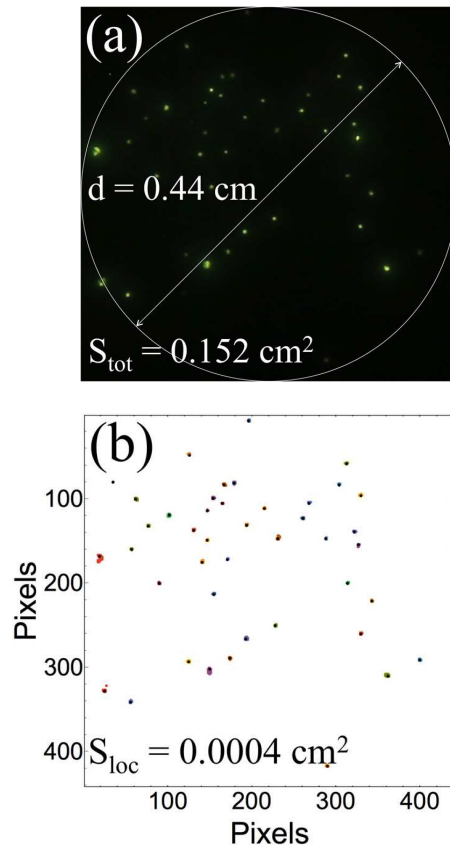


FIG. 4: (a) One exemplary micrograph of the emission pattern of the sample (N)UNCD/Mo/SS, seen on the YAG anode screen at 21.8 μA and 650V, from the dataset **MoSS**, Appendix B. The total cathode area is $S_{cathode} = 0.152 \text{ cm}^2$. (b) The green light emission pattern imaged on the YAG anode screen converted into the actual locally resolved emission area $S_{loc}(E)$ by the clustering algorithm: the total number of pixels clustered together is multiplied by the pixel size in cm^2 , which is evaluated with respect to the known total cathode area. The emission area appears to be only $4 \times 10^{-4} \text{ cm}^2$ at the current of 21.8 μA .

rent density j versus the electric field in Fig.5 by convention, i.e. by dividing the experimentally measured current by the entire cathode area $S_{cathode} = const$

$$j(E) = \frac{I(E)}{S_{cathode}}. \quad (1)$$

The conventional representation makes the samples seem to enable different current densities. This results in somewhat misleading interpretation of data even for the same emitter (N)UNCD/Ni/Mo/SS measured at two different gaps (panels (b) and (c) in Fig.5).

Note, in Figs.5, 7, and 8, the low field vertical markers show the turn-on electric field, i.e. the electric field at which field emission initiates. The higher field markers show the current (and the corresponding electric field) at which the image processing algorithm has detected the first pixel (first pixel detected, f.p.d., voltage ramped

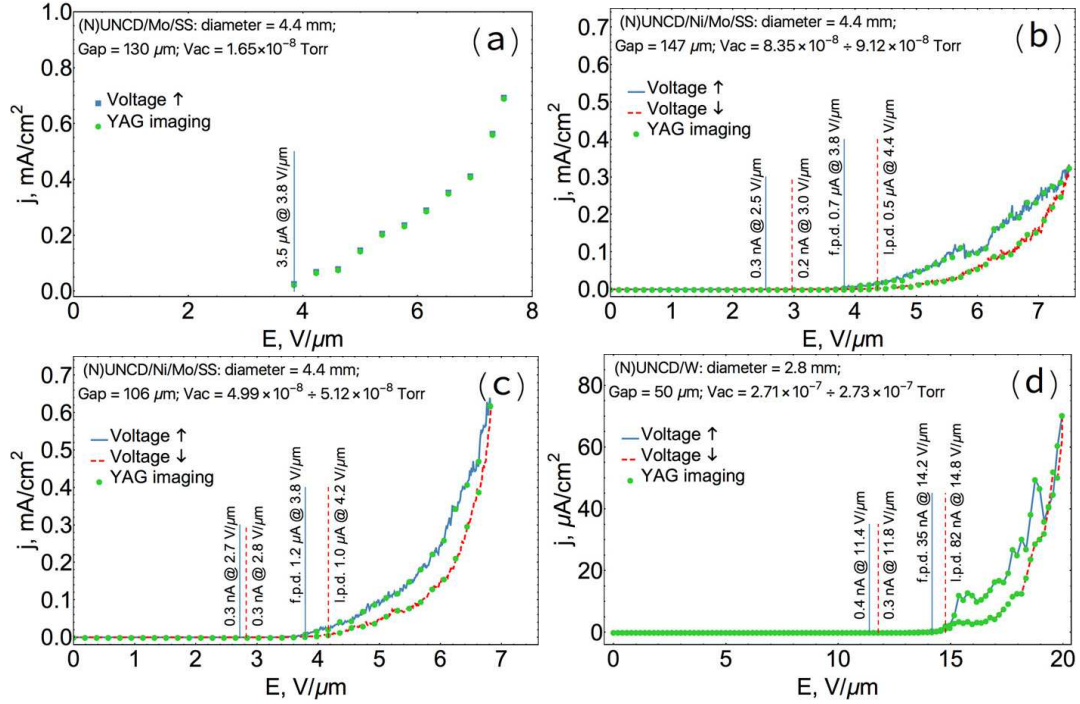


FIG. 5: j - E plots for the datasets (a) **MoSS**, (b) **NiMoSS1**, (c) **NiMoSS2**, and (d) **W**. Current density j is calculated using Eq.1.

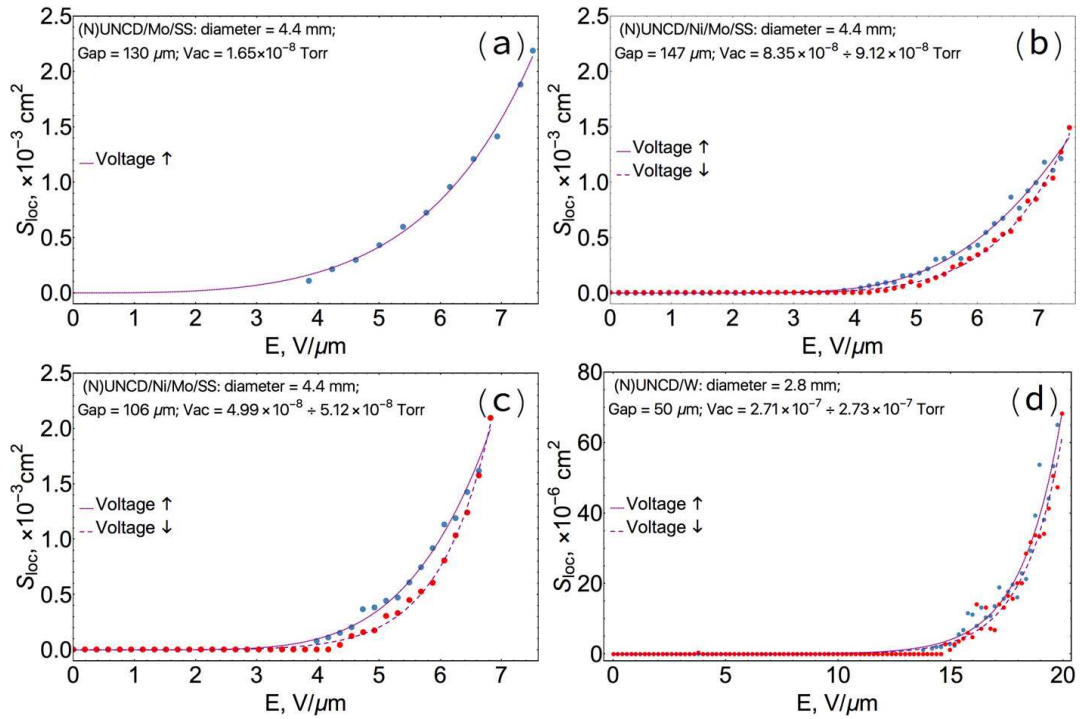


FIG. 6: Dependence of the actual field emission area S_{loc} on the electric field for all the datasets: (a) **MoSS**, (b) **NiMoSS1**, (c) **NiMoSS2**, and (d) **W**. The dependencies $S_{loc}(E)$ were obtained using the developed image processing algorithm.

up) and the last pixel (last pixel detected, l.p.d., voltage ramped down) with the intensity that satisfies Eq.A4 in Appendix A. The datasets in the Appendices B to E start/end with the images before/after which the imaging processor would not detect bright pixels above the background.

After applying the imaging algorithm to the datasets shown in full in Appendices B to E, the locally resolved actual emission area S_{loc} was found to be a dynamic property that strongly depends on the electric field; for all the (N)UNCD field emitters measured. $S_{loc}(E)$ non-linearly but monotonically increased with the applied electric field, as illustrated in Fig.6, as well as monotonically decreased with the electric field swept down to zero following nearly identical non-linear law. The samples on the SS bases had emission area of $\sim 1\%$ of the total cathode area (4.4 mm dia.) at the maximum output current of 100 μA and electric field of about 7 $\text{V}/\mu\text{m}$. The emission area of the sample on W was as small as $\sim 10^{-3}\%$ of the total cathode area (2.8 mm dia.) at the maximum output current of 5 μA and electric field of 20 $\text{V}/\mu\text{m}$.

The apparent inconsistency revealed in Fig.5 vanishes if the experimentally measured current is normalized by the dynamic surface area $S_{loc}(E)$, which was obtained by the least square fitting of the experimental curves using a combined function $S_{loc}(E) = aE^n \exp(bE^m)$

$$j_{cor}(E) = \frac{I(E)}{S_{loc}(E)}, \quad (2)$$

with $S_{loc}(E) \neq const$. The corrected semi-log j_{cor} - E plots are summarized in Fig.7, as well as the comparison between the conventional (left column (a-d)) normalization using $S_{cathode}$ and the newly proposed (right column (a-d)) normalization using $S_{loc}(E)$ is drawn. From Figs.7 and 8, it is seen that all the samples demonstrated saturation behavior. After a very short FN-like dependence manifested as a nearly linear j - E relation (only available for the automatically recorded datasets **NiMoSS1**, **NiMoSS2** and **W**), a strong kink and deviation from the FN law took place. In fact, j_{cor} - E still slowly increases as when plotted in linear coordinates. The lingo *saturation* is used because $\ln(I/E^2)$ indeed saturates with E , as illustrated in Fig.8, because the current increment is the same or smaller than that of E^2 .

Also note, at small voltages applied with no field emission current, $S_{loc}(E) = 0$. In this region, the resulting current density is infinite. To smoothly stitch the parts of the j_{cor} - E curves before and after the turn-on field, the currents $I(E)$ in the sets **NiMoSS1**, **NiMoSS2**, and **W** measured between 0 $\text{V}/\mu\text{m}$ and the sub-nA vertical markers identifying the turn-on field are normalized by $S_{loc}(E) = 2.7 \times 10^{-6} \text{ cm}^2$, $S_{loc}(E) = 7.9 \times 10^{-6} \text{ cm}^2$, and $S_{loc}(E) = 4.4 \times 10^{-7} \text{ cm}^2$, respectively, as obtained by the fitting $S_{loc}(E)$ at the turn-on field point. This yields current densities $\sim 10^{-2} \text{ mA}/\text{cm}^2$. When j is calculated

by the convention with $S_{cathode}(E) = const$, the measured current is normalized by the total cathode surface area of 0.152 cm^2 , or 0.062 cm^2 for **W** dataset. This leads to a few orders of magnitude difference between j and j_{cor} (Fig.7), and sets j_{cor} - E curves higher against j - E curves in FN coordinates in Fig.8.

Most strikingly, it was observed that all j_{cor} - E curves saturated at $\sim 100 \text{ mA}/\text{cm}^2$, despite apparent significant difference was seen from I - E or j - E curves. This leads us to conclude that: (i) the saturation current level of $\sim 100 \text{ mA}/\text{cm}^2$ represents a basic intrinsic property of (N)UNCD films while (ii) the $S_{loc}(E)$ value, i.e. the number of emitting channels available on the surface, is an effect driven by the substrate choice. The obtained results show that the deviation from the FN law onsets (kink point) when the critical current density is achieved regardless of the applied electric field. It is demonstrated that the turn-on electric field threshold and β -factor, representing the FN part of the j - E curve, are independent from the saturation current. This is summarized in Fig.9. The sets **NiMoSS1** and **NiMoSS2** turned on at 2.5 $\text{V}/\mu\text{m}$ while the set **W** required the field of 11-12 $\text{V}/\mu\text{m}$. This means macroscopic roughness (original roughness of the W substrate, Fig.2a) and micro- and submicroscopic topography (clustered spheres of the Ni/Mo/SS substrate, Fig.2b) are not prerequisites for good FE properties. The substrate type is a key factor under the default growth conditions in the CVD reactor. This manifests in the Raman spectra (Fig.2d) as the decreased D/G ratio, from standard 1.6 to 1.4-1.2, suggesting that emission sites and their amount depend on the graphitic fraction in the film. Similar effect was observed by other groups, see for instance Ref. [21] where the increased of amount of the graphitic sp^2 phase led to improved field emission properties of (N)UNCD films as was evaluated by Raman and NEXAFS spectroscopy. The combined locally resolved field emission and Raman microscopy study must be conducted to validate this speculation.

The observed saturation effect places (N)UNCD together with the rest of conventional semiconductors, in which identical effects were reported as early as 1960's [22, 23]. It has been consistently measured until this very day that, in contrast to metals, the FN law breaks down. When plotted in FN, $\ln(j/E^2)$ - $1/E$, coordinates, electric characteristics of semiconductors deviate and rapidly part down from the straight line. There are also a vast number of reports on the saturation effect in carbon-based materials [24-27]. The nature of the saturation plateau was speculated to be due to electron tunneling through multiple barriers in diamond films [26], or most frequently due to the space charge effect [27, 28].

At the same time, in the original work on the space charge effect in field emission [29], current densities as high as $10^7 \text{ A}/\text{cm}^2$ are required to start screening the electric field. Unless extreme localization of emitting centers is assumed, no such current densities are observed in

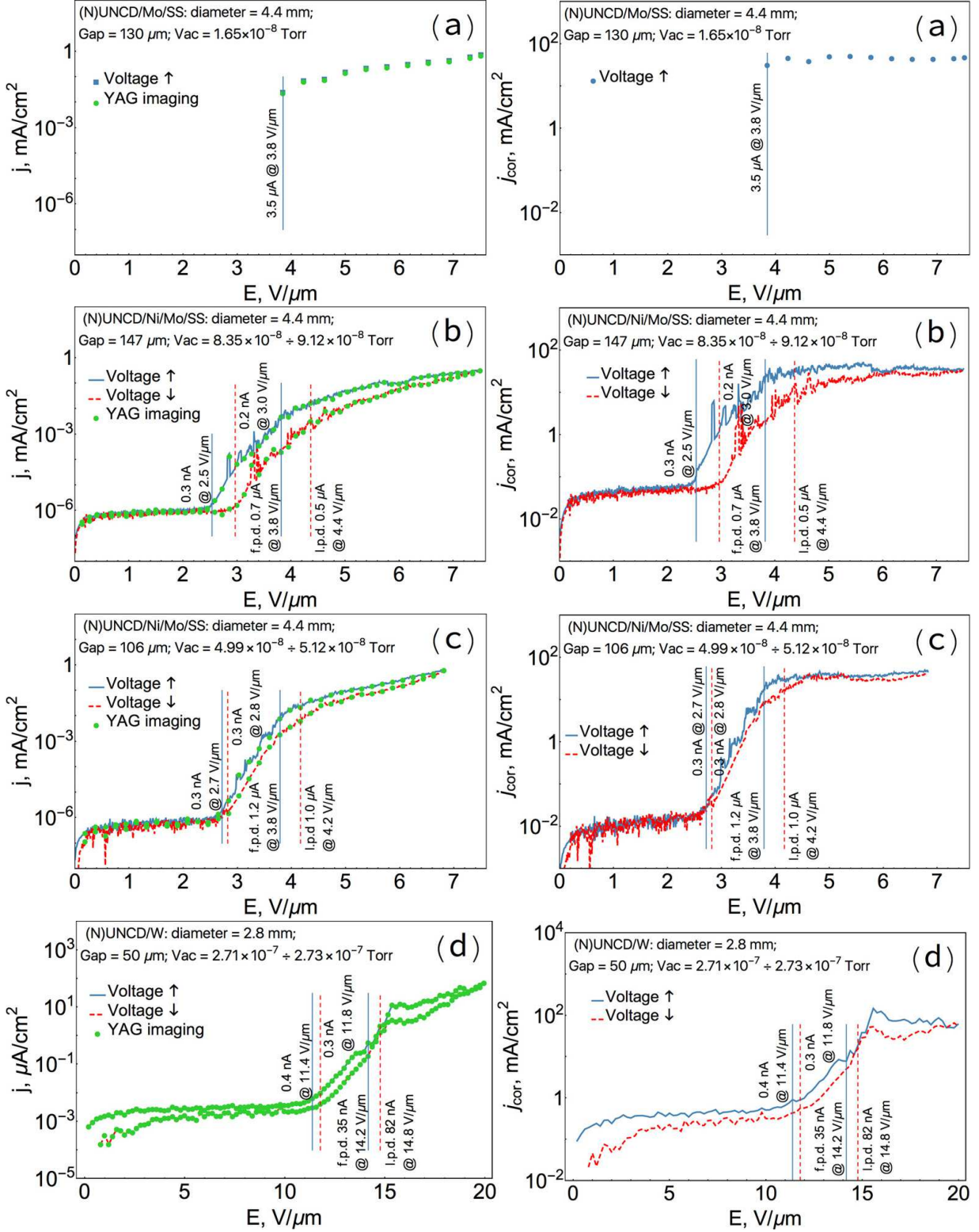


FIG. 7: Semi-log plots of current density as a function of the applied electric field obtained by convention using Eq.1 (j vs. E , (a) to (d) on the left) and by normalizing with $S_{loc}(E)$ using Eq.2 (j_{cor} vs. E , (a) to (d) on the right) for four samples: (a) MoSS, (b) NiMoSS1, (c) NiMoSS2, and (d) W.

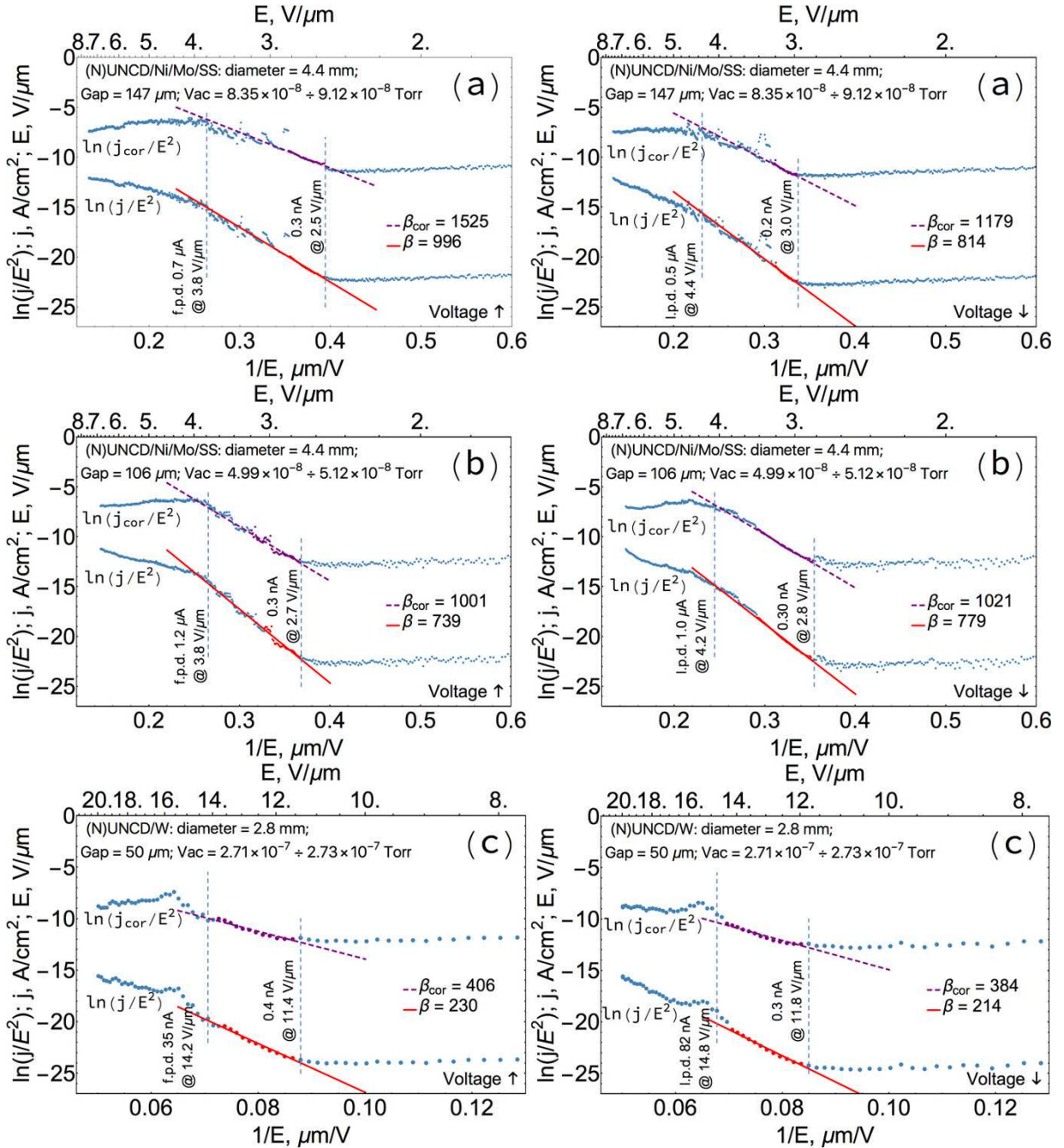


FIG. 8: Comparison between FN plots obtained by convention and by normalizing with $S_{loc}(E)$ for (a) NiMoSS1, (b) NiMoSS2, and (c) W. Left column combines ramp-up FN plots. Right column are ramp-down FN plots. j_{cor} are on top and the convention j are below.

carbon-derived materials. This let us to speculate that the saturation phenomenon in amorphous carbon, polycrystalline diamond and CNT has the same fundamental origin apart from the space charge effect. Further experimental and theoretical work to explain the plateau and its value ~ 100 mA/cm², and investigation of this phenomenon more thoroughly is underway. The developed methodology of determining the actual emission

area $S_{loc}(E)$ makes it possible to study other carbonic field emitters and therefore, e.g., to confirm or reject the hypothesis on the space-charge effect in CNT fibers [27].

There are two other consequences of the imaging experiments that we have conducted. First, the electric characteristics plotted in FN coordinates in Fig.8 suggest a certain increase of the β -factors for the j_{cor} - E curves family because the pre-saturation region was modified af-

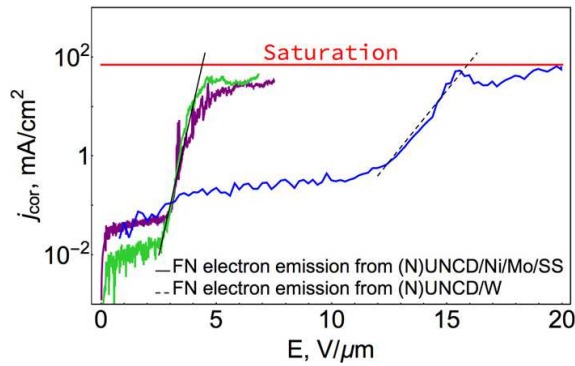


FIG. 9: Comparison plot of the sets **NiMoSS1** (purple curve) **NiMoSS2** (green curve) and **W** (blue curve). Black solid and dashed lines are to crudely depict FN curve of the j - E curves.

ter correcting with $S_{loc}(E)$. Second, the hysteresis of j - E characteristics in Fig.5, which is commonly reported by many other groups (see e.g. Ref.[27]), is not caused by the hysteresis of the emission area within accuracy of our experiment and image processing as we do not observe significant hysteresis of the $S_{loc}(E)$, when the voltage is ramped up and down as evidenced in Fig.6.

IV. SUMMARY

An image processing concept and methodology were developed and implemented, in order to extract the actual, locally resolved, effective emission area of (N)UNCD films from emission pattern micrographs acquired using a field emission projection microscope, concurrently with current-voltage characteristics. It was shown that the effective emission area depends non-linearly on the applied electric field and repeatedly increases/decreases as the field is ramped up/down.

By normalizing the measured current by the dynamic emission area rather than by the constant entire cathode area and analyzing the resulting j - E curves, a few important conclusions were made: (i) semi-metallic (N)UNCD saturates similarly as semiconductors; (ii) in topographically uniform (N)UNCD thin films, field emission is not uniform; (iii) field emission current density is limited at ~ 100 mA/cm²; this is specific to (N)UNCD, regardless of substrate; (iv) roughness and topography are not prerequisites for good FE properties.

Additionally, the proposed concept of microscopy and image processing has potential as a novel express technological procedure to accurately quantify effects in as-synthesized emitters and upon their surface termination/functionalization.

Acknowledgments. The authors would like to thank Dr Igor Volkov (GWU) for his help with implementation of the clustering algorithm and Dr. George Younes

(GWU) for valuable discussions.

Euclid TechLabs was supported by the Office of Nuclear Physics of DOE through a Small Business Innovative Research grant #DE-SC 0013145.

Samples synthesis, SEM and Raman measurements were conducted in the Center for Nanoscale Materials at Argonne National Laboratory. Use of the Center for Nanoscale Materials, an Office of Science user facility, was supported by the U.S. Department of Energy, Office of Science, Office of Basic Energy Sciences, under Contract No. DE-AC02-06CH11357.

S.S. Baturin was supported by NSF grants #PHY-1535639 and #PHY-1549132 during the time of preparing the manuscript for publication.

* Electronic address: chubenko@gwu.edu

† Electronic address: sergey.v.baryshev@gmail.com

- [1] R.H. Fowler and L. Nordheim, Proc. Royal Soc. A **119**, 173 (1928).
- [2] P. Serbun, A systematic investigation of carbon, metallic and semiconductor nanostructures for field-emission cathode applications, Ph.D. thesis, University of Wuppertal (2014).
- [3] P. Serbun, B. Bornmann, A. Navitski, G. Mller, C. Prommesberger, C. Langer, F. Dams, and R. Schreiner, J. Vac. Sci. Technol. B **31**, 02B101 (2013).
- [4] R. Schreiner, C. Langer, C. Prommesberger, S. Mingels, P. Serbun, and G. Muller, IEEE Proc. doi:10.1109/IVNC.2013.6624721 (2013).
- [5] D. Lysenkov and G. Muller, International J. Nanotechnology **2**, 239 (2005).
- [6] A.G. Kolosko, E.O. Popov, S.V. Filippov, and P.A. Romanov, J. Vac. Sci. Technol. B **33**, 03C104 (2015).
- [7] S. A. Lyashenko, A. P. Volkov, R. R. Ismagilov, and A. N. Obraztsov, Tech. Phys. Lett. **35**, 249 (2009).
- [8] M.L. Terranova, S. Orlanducci, M. Rossi, and E. Tamburri, Nanoscale **7**, 5094 (2015).
- [9] A.V. Sumant, O. Auciello, R.W. Carpick, S. Srinivasan, and J.E. Butler, MRS Bull. **35**, 281 (2011).
- [10] S.S. Baturin and S.V. Baryshev, Rev. Sci. Instrum. **88**, 033701 (2017).
- [11] K.J. Pérez Quintero, S. Antipov, A.V. Sumant, C. Jing, and S.V. Baryshev, Appl. Phys. Lett. **105**, 123103 (2014).
- [12] S.V. Baryshev, S. Antipov, J. Shao, C. Jing, K.J. Prez Quintero, J. Qiu, W. Liu, W. Gai, A.D. Kanareykin, and A.V. Sumant, Appl. Phys. Lett. **105**, 203505 (2014).
- [13] J. Birrell, J.E. Gerbi, O. Auciello, J.M. Gibson, J. Johnson, and J.A. Carlisle, Diamond Relat. Mater. **14**, 86 (2005).
- [14] C.-C. Teng, S.-M. Song, C.-M. Sung, and C.-T. Lin, J. Nanomaterials **2009**, 621208 (2009).
- [15] F. Klauser, D. Steinmüller-Nethl, R. Kaindl, E. Bertel, and N. Memmel, Chemical Vapor Deposition **16**, 127 (2010).
- [16] F.P. Gavril, V.M. Kaspi, and P.M. Woods, Astrophys. J. **607**, 959 (2004).
- [17] P.-K. Chan, S.-H. Cheng, and T.-C. Poon, J. Electronic

- Imaging **16**, 043003 (2007).
- [18] A. Khotanzad and A. Bouarfa, *Pattern Recognition* **23**, 961 (1990).
 - [19] A.F. Zepka, J.M. Cordes, and I. Wasserman, *Astrophys. J.* **427**, 438 (1994).
 - [20] A. Rodriguez and A. Laio, *Science* **344**, 1492 (2014).
 - [21] K.J. Sankaran, J. Kurian, H.C. Chen, C.L. Dong, C.Y. Lee, N.H. Tai, and I.N. Lin, *J. Phys. D* **45**, 365303 (2012).
 - [22] J.R. Arthur, *J. Appl. Phys.* **36**, 3221 (1965).
 - [23] L.M. Baskin, O.I. Lvov, and G.N. Furse, *Phys. Status Solidi B* **47**, 49 (1971).
 - [24] D. Varshney, C. Venkateswara Rao, M. J. F. Guinel, Y. Ishikawa, B. R. Weiner, and G. Morell, *J. Appl. Phys.* **110**, 044324 (2011).
 - [25] C. Ducati, E. Barborini, P. Piseri, P. Milani, and J. Robertson, *J. Appl. Phys.* **92**, 5482 (2002).
 - [26] M. Liao, Z. Zhang, W. Wang, and K. Liao, *J. Appl. Phys.* **84**, 1081 (1998).
 - [27] M. Cahay, P.T. Murray, T.C. Back, S. Fairchild, J. Boeckl, J. Bulmer, K.K.K. Koziol, G. Gruen, M. Sparkes, F. Orozco, and W. O'Neill, *Appl. Phys. Lett.* **105**, 173107 (2014).
 - [28] N.S. Xu, J. Chen, and S.Z. Deng, *Appl. Phys. Lett.* **76**, 2463 (2000).
 - [29] J.P. Barbour, W.W. Dolan, J.K. Trolan, E.E. Martin, and W.P. Dyke, *Phys. Rev.* **92**, 45 (1953).

Appendix A. The automated image processing algorithm used to process all datasets of the field emission pattern micrographs.

The routine consists of the data preprocessing, local maxima search, clustering, and segmentation. The implementation of each of the steps is described as follows.

A1. Data Preprocessing

The first step towards the image processing is data preparation. The input data is an actual RGB micrograph as shown in Fig.A1. Built-in Mathematica functions, namely *ColorConvert* and *ImageData*, are used to convert RGB images into grayscale, represented in shades of gray between 0 (black) and 1 (white), and to retrieve the obtained image data in the form of a 2D array of pixel values (intensities), respectively. The intensity is represented by $I_{i,j}$ with $i = 1, 2, \dots, i_{max}$, and $j = 1, 2, \dots, j_{max}$, where i_{max} and j_{max} stand for the image dimensions measured in pixels as shown in Fig.A2 (typically, our images are 442×442 pixels in size). As we employ Poisson distribution for image processing, we can further convert intensities into a 2D array of integer numbers $0, 1, 2, \dots, I_{max}$. To achieve this, each value in the dataset is subtracted by the minimal intensity I_{min} determined as $Min(I_{i,j} | i = 1, \dots, i_{max}; j = 1, \dots, j_{max})$ and divided by the minimal intensity difference in the array δI_{min} determined as $Min(Abs(I_{m,n} - I_{l,k}) | m, l = 1, \dots, i_{max}; n, k = 1, \dots, j_{max})$.

$$I_{i,j} = \frac{I_{i,j} - I_{min}}{\delta I_{min}}. \quad (A1)$$

A2. Local Maxima Search

Here we use the idea that the local maximum is defined as a pixel with an intensity larger than that of any other neighbor and located at a relatively large distance from pixels with higher intensities [20]. The local maxima search routine involves calculating the distance to the nearest pixel with higher intensity. The distance is assumed to be the Euclidian distance r between two pixels $I_{m,n}$ and $I_{l,k}$ with coordinates (m, n) and (l, k) , respectively

$$r = \sqrt{(m - l)^2 + (n - k)^2} \quad (A2)$$

with m and l running over 1 to i_{max} , and n and k running over 1 to j_{max} . This procedure is accomplished for each pixel $I_{i,j}$ by examining the intensities of all neighbor pixels, which lie inside the circle of radius r_{cr} centered at the particular pixel. In our case, for a 442×442 pixel array, we use $r_{cr} = 10$. To illustrate the general approach,

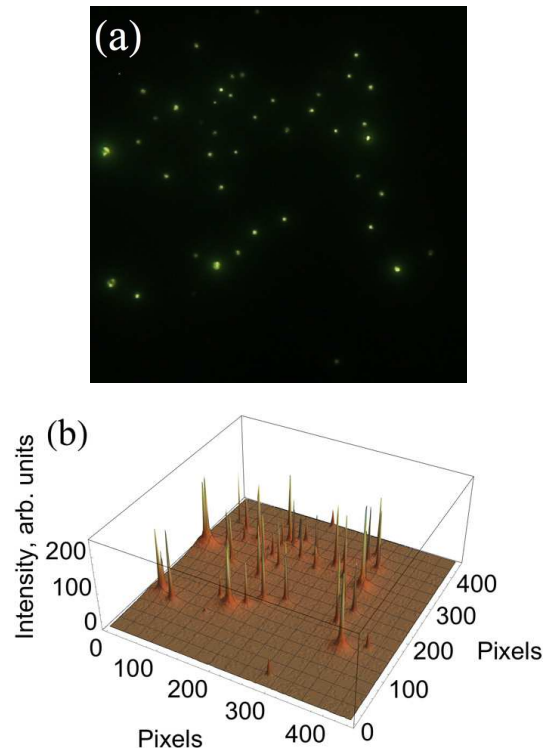


FIG. A 1: (a) An example of a typical input image, field emission pattern taken at the applied field strength of $5 \text{ V}/\mu\text{m}$ during $I - V$ measurements. (b) 3D plot of the resulting data array.

	1	...	j	...	j_{max}
1	$I_{1,1}$...	$I_{1,j}$...	$I_{1,j_{max}}$
⋮	⋮		⋮		⋮
i	$I_{i,1}$...	$I_{i,j}$...	$I_{i,j_{max}}$
⋮	⋮		⋮		⋮
i_{max}	$I_{i_{max},1}$...	$I_{i_{max},j}$...	$I_{i_{max},j_{max}}$

FIG. A 2: Convention for labeling the indexes in the dataset of pixel values $I_{i,j} = 0, 1, 2, \dots, I_{max}$.

let us consider a small part of a dataset. Fig.A3 illustrates the closest brighter pixel search in a 15×15 pixel array. For most pixels, the nearest brighter pixels will lie at a distance $r = 1$. For example, Fig.A3a shows the closest brighter pixel search for the pixel $I_{1,1}$, where we highlight in green the search area. It can be seen that the closest brighter pixel $I_{2,1} = 6$ is located at $r = 1$, whereas pixel $I_{6,4} = 136$ does not have any brighter pixels in the highlighted neighborhood (Fig.A3b). We define such pixels as *the brightest in the neighborhood*. Next, for each of the brightest in the neighborhood pixels, we calculate the distance to the closest brighter pixel in the list of

the brightest pixels. For the pixel with highest intensity (global maximum), we take the distance to the closest pixel in the list of the brightest pixels. At the end of this routine, each pixel of a 2D array is associated with its own intensity $I_{i,j}$ and distance to the nearest brightest pixel $r_{i,j}$.

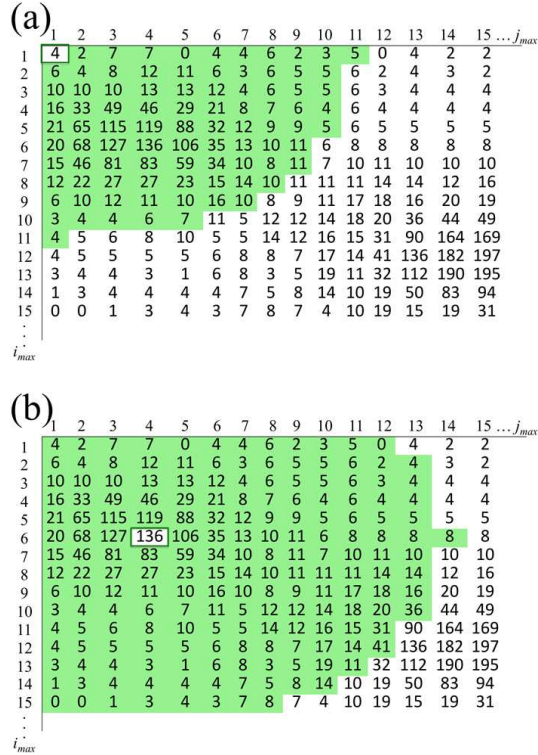


FIG. A 3: Illustration of the closest brighter pixel search algorithm. (a) Most of the pixels have their brighter neighbors at relatively small distances. Pixel $I_{1,1} = 4$ has its closest brighter neighbor $I_{2,1} = 6$ located at $r = 1$. (b) Pixel $I_{6,4} = 136$ is the brightest in the neighborhood. The closest brighter pixel $I_{12,15} = 197$ is located at $r = 12.53$, which is out of r_{cr} . The pixel $I_{12,15}$ is also defined as the brightest in its neighborhood.

It is convenient to plot the distance $r_{i,j}$ as a function of intensity $I_{i,j}$ for each pixel. We will further call this representation the decision plot as defined by Rodriguez and Laio [20]. Fig.A4 shows the decision plot for the image in Fig.A1a. It can be seen that only some of the pixels possess a combination of high intensity and a distance much larger than r_{cr} . These are *local maxima*.

In order to completely automate the local maxima search, we need to define two parameters, the minimal distance D_{min} and the minimal intensity I_{min} . The pixel, which possesses these values, will be classified as a local maximum. The choice of D_{min} primarily depends on the image resolution. Images with higher resolution will require a larger value of this parameter. It was found that for 442×442 pixel image, $D_{min} = 7$ is an appropriate choice, whereas the choice of I_{min} requires an estimation

of the background level.

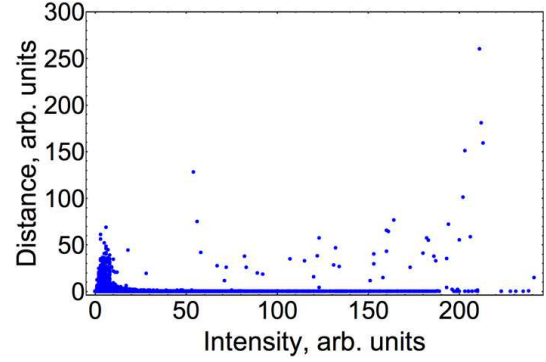


FIG. A 4: An example of the decision plot for the image shown in 1a.

Each pixel intensity $I_{i,j}$ is a sum of both the true signal, the light emission from a discrete emission site, the background, the emission from other emission sites, and the noise contributed by the light detection system itself. One common method of separating the signal from the background is based on an assumption that the background follows a Poisson distribution [16, 19]. The probability of observing a pixel with a random intensity $I_{i,j}$, when the mean intensity is λ , can be written as

$$P_{i,j} = \frac{\lambda^{I_{i,j}} e^{-\lambda}}{I_{i,j}!}. \quad (\text{A3})$$

Pixels that satisfy the condition

$$P_{i,j} \leq 0.01/N, \quad (\text{A4})$$

where N is the total number of pixels, are assumed to be the meaningful signal and are subject to further examination [16]. Since there are several emission sites on the picture, each with a different brightness, the background level can be overestimated. Therefore, pixels that satisfy the above condition are removed from the dataset and the procedure is repeated until there are no additional pixels of interest. The background level is then determined by the largest element of a final data list. The histogram in Fig.A5 illustrates an automatically determined background level. Pixels with $I_{i,j} \geq 23$ and $r_{i,j} \geq 7$ are local maxima and are marked in red on the decision plot (Fig.A6).

A3. Clustering

The methodology described above determines the number of local maxima, i.e. the number of seeding centers around which clusters will be built. The clustering procedure is performed by linking the pixels around the local maxima together. For each local maximum, the algorithm seeks the pixels for which this particular local

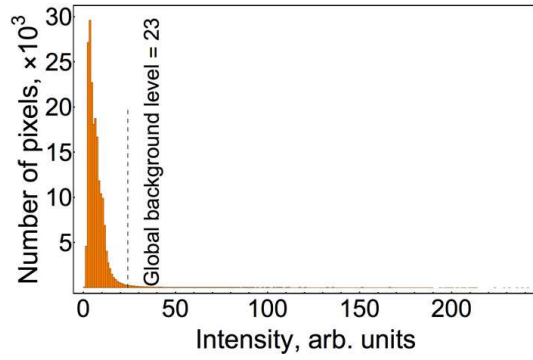


FIG. A 5: Histogram of data for the image in Fig.A1a. The algorithm picks pixels until the condition (A4) holds true.

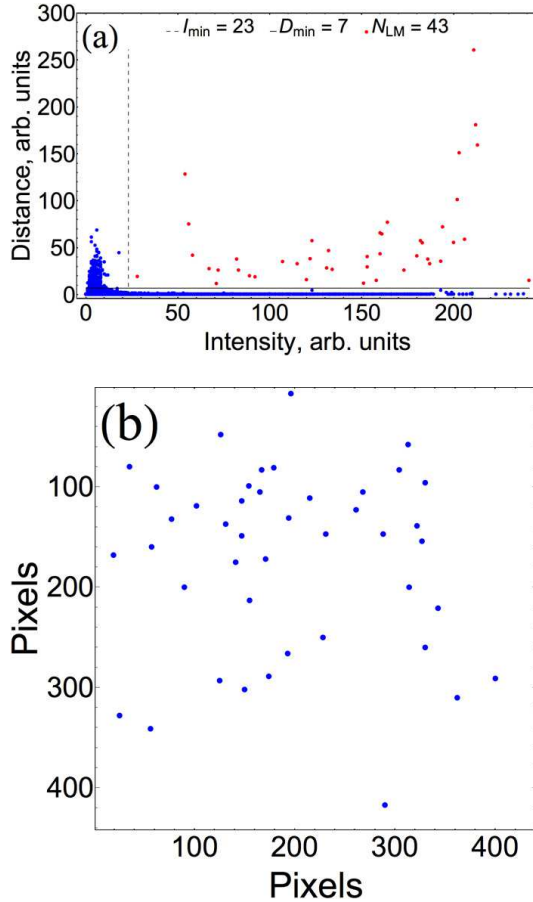


FIG. A 6: (a) Decision plot for the image presented in Fig.A1a with automatically calculated number of local maxima N_{LM} . Red dots correspond to Poisson distribution of a final dataset (background noise). (b) The pixel map of the found local maxima.

maximum is a brighter pixel and attaches these pixels to the local maximum. Attached pixels, in turn, have pixels for which they are brighter neighbors (Fig.A7). The procedure is repeated for each local maximum until no more corresponding pixels are found. At this point, clusters are complete. An example of a 442×442 pixel independent

cluster family is shown in Fig.A8. Independent clusters around local maxima are color-coded.

	1	2	3	4	5	6	7	8	9	10	11	12	13	14	15	...	j_{max}
1	4	2	7	7	0	4	4	6	2	3	5	0	4	2	2		
2	6	4	8	12	11	6	3	6	5	5	6	2	4	3	2		
3	10	10	10	13	13	12	4	6	5	5	6	3	4	4	4		
4	16	33	49	46	29	21	8	7	6	4	6	4	4	4	4		
5	21	65	115	119	88	32	12	9	9	5	6	5	5	5	5		
6	20	68	127	136	106	35	13	10	11	6	8	8	8	8	8		
7	15	46	81	83	59	34	10	8	11	7	10	11	10	10	10		
8	12	22	27	27	23	15	14	10	11	11	11	14	14	12	16		
9	6	10	12	11	10	16	10	8	9	11	17	18	16	20	19		
10	3	4	4	6	7	11	5	12	12	14	18	20	36	44	49		
11	4	5	6	8	10	5	5	14	12	16	15	31	90	164	169		
12	4	5	5	5	5	6	8	8	7	17	14	41	136	182	197		
13	3	4	4	3	1	6	8	3	5	19	11	32	112	190	195		
14	1	3	4	4	4	4	7	5	8	14	10	19	50	83	94		
15	0	0	1	3	4	3	7	8	7	4	10	19	15	19	31		
...																	
i_{max}																	

FIG. A 7: Illustration of a clustering algorithm. Different colors represent a formation of two different clusters around two local maxima.

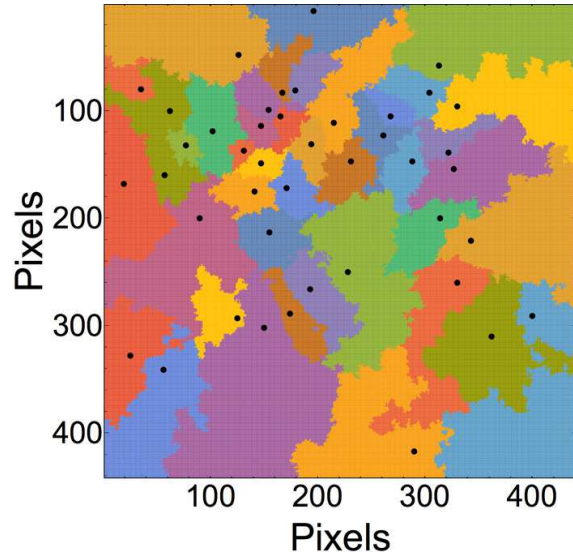


FIG. A 8: Final result of a clustering procedure.

A4. Segmentation

After clusters are formed around each local maximum, we perform a segmentation procedure to decide how many pixels belong to each emission site and therefore to evaluate the total emission area at a given electric field. In order to estimate a local background, we assume that each emission site has a Gaussian shape and use a 2D Gaussian function to fit each peak

$$f(x, y) = Ae^{-\frac{(x-x_0)^2}{2\sigma_x^2} - \frac{(y-y_0)^2}{2\sigma_y^2}} + B_{loc}. \quad (A5)$$

Here coefficients A and B_{loc} are the amplitude and local background, respectively, x_0 and y_0 define the pixel posi-

tion of a local maximum, and σ_x and σ_y are the standard deviations in perpendicular directions (Fig.A9).

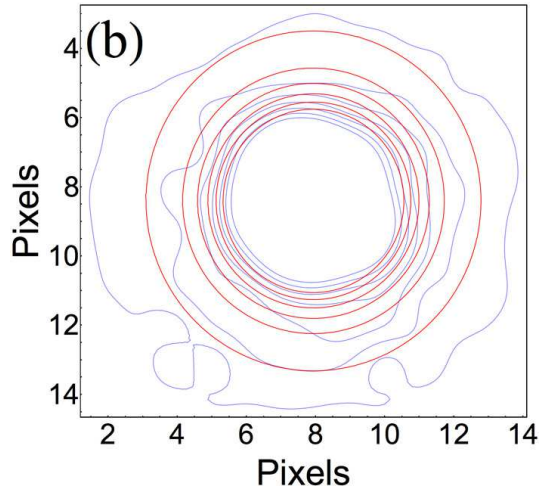
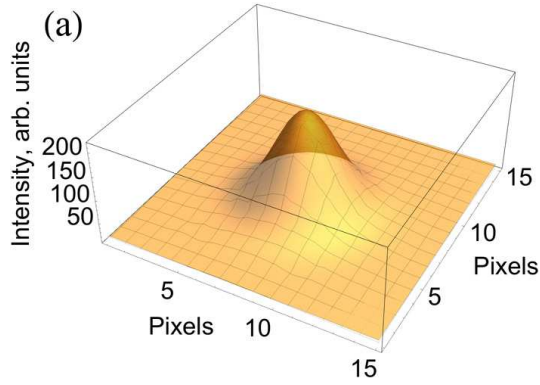


FIG. A 9: (a) An emission peak with a fitting Gaussian curve and (b) a corresponding contour plot.

Further, we select only the pixels with intensity within one standard deviation away from the mean, which means that only the pixels that exceed the threshold

$$I_{th} = 0.61I_{max} + 0.4B_{loc} \quad (A6)$$

contribute to the emission area. Here I_{max} is the local maximum intensity and B_{loc} is the local background (see Fig.A10).

The pixel size in cm^2 is referenced to the full image size in pixels and the known diameter of the (N)UNCD cathode, 0.44 or 0.28 cm. The product of the total number of pixels combined by the clustering procedure and the pixel size in cm^2 provides the total emission area per micrograph in the datasets shown in the Appendices B to E.

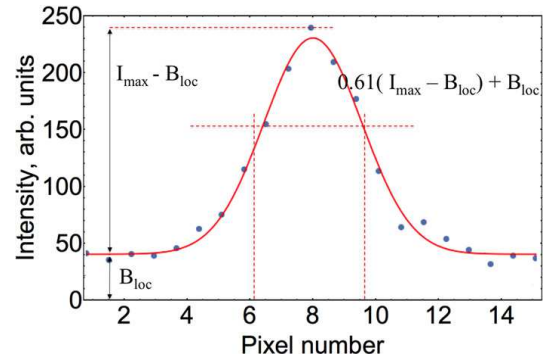
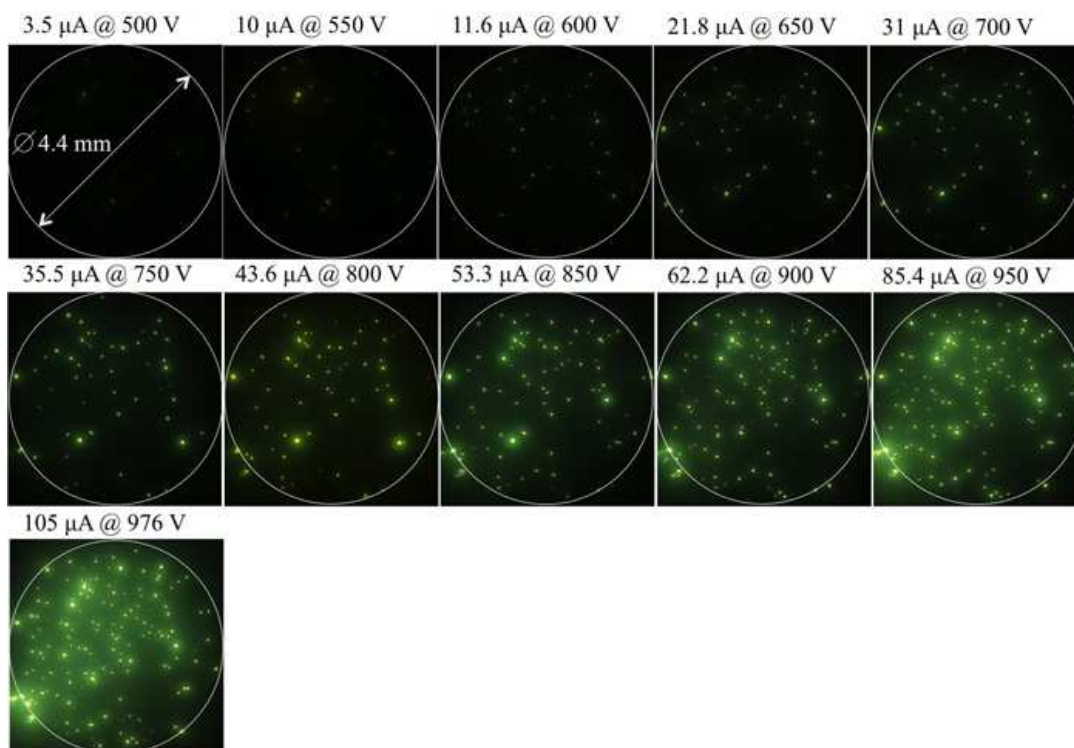
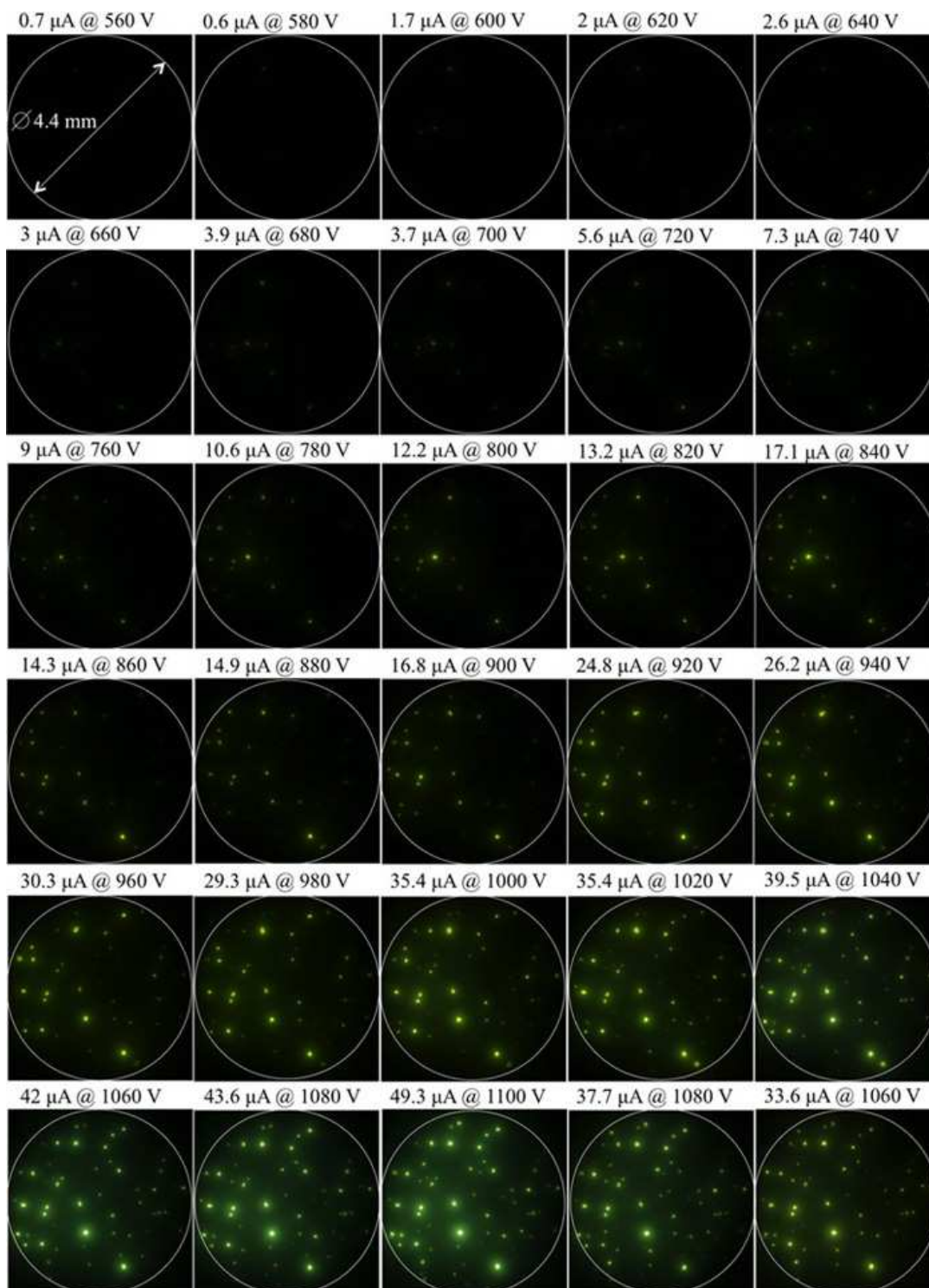


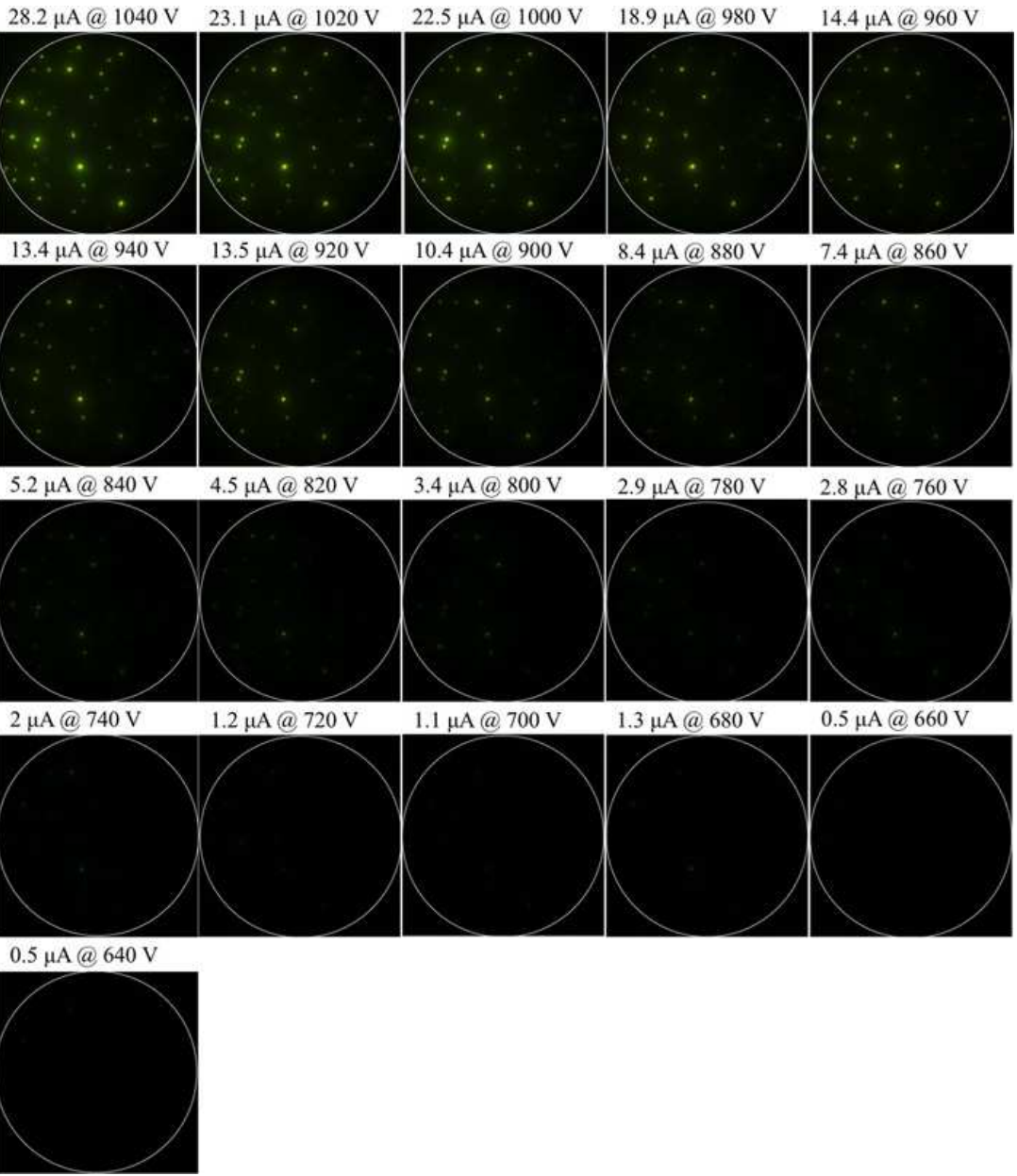
FIG. A 10: Result of a clustering algorithm.

Appendix B. The micrograph set for (N)UNCD/Mo/SS measured at an inter-electrode gap (UNCD-YAG) of 130 μm and pressure 1.65×10^{-8} Torr. All 11 images were acquired in the course of ramping the voltage up.

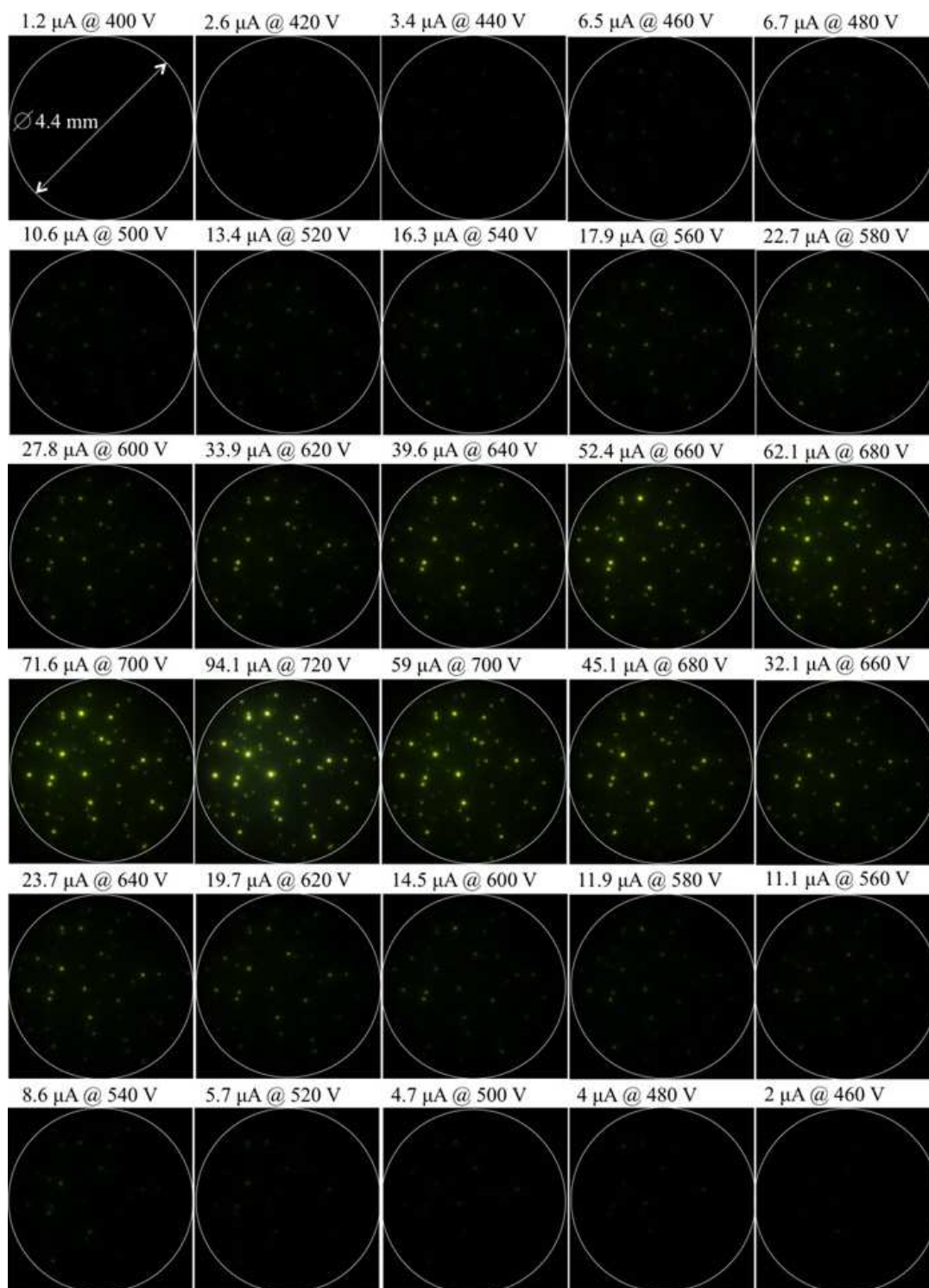


Appendix C. The micrograph set for (N)UNCD/Ni/Mo/SS measured at an inter-electrode gap (UNCD-YAG) of $147\ \mu\text{m}$ and pressure about 9×10^{-8} Torr. The presented 51 images are those on which the image processing algorithm has detected high intensity pixels above the background threshold. The full set was recorded in the course of ramping the voltage up (0 to 1,100 V with a step of 20 V) and then down (1,100 to 0 V with a step of 20 V).





Appendix D. The micrograph set for (N)UNCD/Ni/Mo/SS measured at an inter-electrode gap (UNCD-YAG) of $106\ \mu\text{m}$ and pressure about 5×10^{-8} Torr. The presented 30 images are those on which the image processing algorithm has detected high intensity pixels above the background threshold. The full set was recorded in the course of ramping the voltage up (0 to 720 V with a step of 20 V) and then down (720 to 0 V with a step of 20 V).



Appendix E. The micrograph set for (N)UNCD/W measured at an inter-electrode gap (UNCD-YAG) of $50\ \mu\text{m}$ and pressure about 3×10^{-7} Torr. The presented 56 images are those on which the image processing algorithm has detected high intensity pixels above the threshold. The full set was recorded in the course of ramping the voltage up (0 to 1,000 V with a step of 10 V) and then down (1,000 to 0 V with a step of 10 V).

